

ARTICLE OPEN

Composite topological nodal lines penetrating the Brillouin zone in orthorhombic AgF_2 Dexi Shao¹, Huaiqiang Wang¹, Tong Chen¹, Pengchao Lu¹, Qinyan Gu¹, Li Sheng^{1,2}, Dingyu Xing^{1,2} and Jian Sun^{1,2} 

It has recently been found that nonsymmorphic symmetries can bring many exotic band crossings. Here, based on symmetry analysis, we predict that materials with time-reversal symmetry in the space group of $Pbca$ (No. 61) possess rich symmetry-enforced band crossings, including nodal surfaces, fourfold degenerate nodal lines and hourglass Dirac loops, which appear in triplets as ensured by the cyclic permutation symmetry. We take $Pbca$ AgF_2 as an example in real systems and studied its band structures with ab initio calculations. Specifically, in the absence of spin-orbit coupling (SOC), besides the above-mentioned band degeneracies, this system features a nodal chain and a nodal armillary sphere penetrating the Brillouin zone (BZ). While with SOC, we find a new configuration of the hourglass Dirac loop/chain with the feature traversing the BZ, which originates from the splitting of a Dirac loop confined in the BZ. Furthermore, guided by the bulk-surface correspondence, we calculated the surface states to explore these bulk nodal phenomena. The evolution of these interesting nodal phenomena traversing the BZ under two specific uniaxial strains is also discussed.

npj Computational Materials (2019)5:53; <https://doi.org/10.1038/s41524-019-0190-3>

INTRODUCTION

Topological materials have attracted great interest both theoretically and experimentally^{1–3} since the proposal of topological insulators (TIs) in 2005.⁴ Generally speaking, topological materials can be classified into gapped phases, such as TIs and topological superconductors (TSCs),^{1,2} and gapless phases consisting of various topological semimetals (TSMs), such as Weyl semimetals (WSMs),^{5–27} Dirac semimetals (DSMs),^{28–43} nodal-line semimetals (NLSMs),^{44–53} and nodal surface semimetals (NSSMs),^{54–58} etc. Symmetries play important roles in the classification of topological phases. One of the celebrated examples is the “periodic table” of noninteracting TIs and topological superconductors (TSCs) characterized by time-reversal symmetry (TRS), particle-hole symmetry, and chiral symmetry.^{59,60} Later, the notion of crystal symmetries has given rise to the discovery of topological crystalline insulators (TCIs).^{59,61–65} Quite recently, guided by group representation theory, researchers have shown that nonsymmorphic symmetries can bring many more fancy degeneracies in the band structures, say, unconventional new fermions beyond Dirac and Weyl fermions.^{34,66–69}

Depending on the dimension (n) of each band-crossing, there exist three types of nodes in TSMs, namely, nodal points with $n = 0$, nodal lines with $n = 1$ and nodal surfaces with $n = 2$, as schematically shown in Fig. 1. Through bulk-surface correspondence, these bulk nodes can manifest themselves by the emergence of certain surface states, such as Fermi arcs in WSMs^{5,70} and drumhead surface states in NLSMs.^{16,44–46} Moreover, these TSMs can exhibit exotic transport phenomena, including negative magnetoresistance and chiral magnetic effect.^{71–81} However, nodal features of the TSMs revealed in most previous works are confined within the BZ, while few cases with their nodes penetrating the BZ are reported.^{50,82}

In this work, based on symmetry analysis, we propose that materials in the space group of $Pbca$ possess rich nodal features as follows. Without SOC, there exist nodal surfaces and fourfold degenerate nodal lines surrounding all the boundary surfaces and edge ridges of the BZ, respectively. When SOC is taken into consideration, we predict that there is a nodal hourglass Dirac loop on each surface of the BZ. It should be emphasized that all of the above-mentioned nodal configurations are symmetry-enforced and appear in triplets as a result of the cyclic permutation symmetry.

With both ab initio calculations and tight-binding analysis, we have taken the orthorhombic AgF_2 as a candidate material to justify the theoretical predictions. It is worth mentioning that besides the above-mentioned nodal features, something more interesting appears in this system. Firstly, without SOC, additional band crossings appear in the geometry of nodal chains and nodal “armillary” spheres penetrating the BZ. The nodal chain and the nodal armillary sphere can be characterized by the $2 \times \mathbb{Z}^3$ and the $2 \times \mathbb{Z}^3 \oplus 2 \times \mathbb{Z}^3$ indices, respectively, with each of the three integers in “ \mathbb{Z}^3 ” depicting the number of times the nodal loop winds around the BZ along one of the three directions. Secondly, when SOC is taken into consideration, we find one of the closed three nodal hourglass Dirac loops in theory splits into two loops stretching across the BZ. Furthermore, both the two touch with a third closed hourglass Dirac loop, forming a novel hourglass Dirac chain traversing the BZ. In addition, the corresponding surface states are also presented to explore the intriguing topological phase and the corresponding physics. Finally, we give a short discussion on the robustness of these nodal geometries under two specific uniaxial strains. The coexistence of multiple exotic nodal configurations with and without SOC makes this system quite

¹National Laboratory of Solid State Microstructures and Department of Physics, Nanjing University, 210093 Nanjing, China and ²Collaborative Innovation Center of Advanced Microstructures, 210093 Nanjing, China

Correspondence: Jian Sun (jiansun@nju.edu.cn)

Received: 16 December 2018 Accepted: 2 April 2019

Published online: 23 April 2019

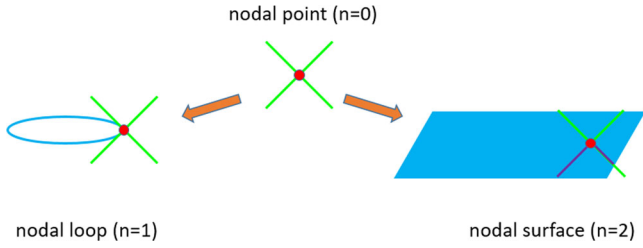


Fig. 1 Schematic illustrations of band crossings in the geometry of nodal point ($n = 0$), nodal-line ($n = 1$), and nodal surface ($n = 2$)

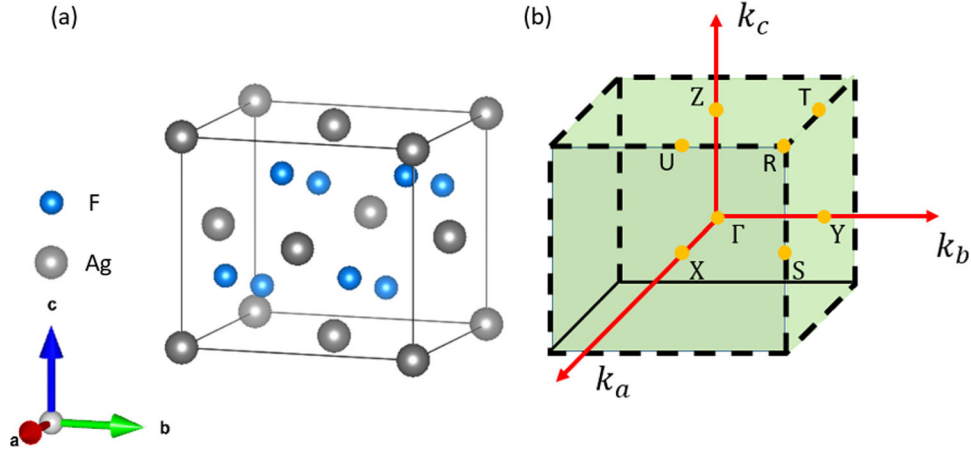


Fig. 2 **a** Crystal structure of AgF_2 at the ambient pressure with $Pbca$ symmetry. Ag and F atoms occupy the 4a (0, 0, 0) and 8c (0.306, 0.128, 0.184) sites, respectively. **b** The corresponding Brillouin zone (BZ). The viridescent shadow planes on the surfaces of the BZ represent the node-surface structures while the bold black dashed edge lines represent the quadruply degenerated nodal lines in the absence of SOC

distinctive, which uncovers an unknown class of topological phases.

RESULTS AND DISCUSSIONS

Nodal phenomena without SOC: symmetry-enforced nodal surfaces and fourfold nodal lines

Space group $Pbca$ contains three skew-axis, the inversion and three glide-mirror symmetries, as shown in Table 1. The subscripts satisfy $(\alpha, \beta) = \{(x, y); (y, z); (z, x)\}$, which present a cyclic permutation relation.

Without SOC, we will first demonstrate that all bands are doubly degenerate on the $k_\alpha = \pi$ ($\alpha = x, y, z$) planes, thus forming the so-called nodal surfaces, shown as the viridescent shadow planes in Fig. 2b. These nodal surfaces are found to be symmetry-enforced as follows. Define three new anti-unitary operators as

$$\Theta_\alpha = R_{2,\alpha} * T, \alpha = \{x, y, z\}, \quad (1)$$

which satisfy $\Theta_\alpha^2 = R_{2,\alpha}^2 T^2 = -1$ for both cases with and without SOC. It is evident that the plane $k_\alpha = \pi$ are Θ_α invariant, and analogous to the well-known Kramers degeneracy, Θ_α can thus ensure the above three nodal surfaces encircling the whole BZ.

In addition, we will show that there exist three robust fourfold degenerate nodal lines along all the edge lines $k_\alpha = k_\beta = \pi$ with $\alpha, \beta = \{x, y, z\}$. For example, we consider the $S - R$ line with $k_x = k_y = \pi$, which is an invariant subspace of $\tilde{M}_{x,y}$ and $\tilde{M}_z^* T$. Similar to the discussion in the X_3SiTe_6 ,⁸³ four orthogonal states labeled as $\{|\mu\rangle, \tilde{M}_z * T|\mu\rangle, \tilde{M}_y|\mu\rangle, \tilde{M}_y\tilde{M}_z * T|\mu\rangle\}$ ⁸³ form a degenerate quartet for \vec{k} points lying on the $S - R$ line, thus protecting the fourfold band degeneracies. Furthermore, due to the cyclic permutation relation,

Operators	Symmetry representation
E	$\{1 0\}$
$\tilde{R}_{2\alpha}$	$\{R_{2\alpha} \frac{1}{2}(a_\alpha + a_\beta)\}$
P	$\{-1 0\}$
\tilde{M}_α	$\{M_\alpha \frac{1}{2}(a_\alpha + a_\beta)\}$

there should also exist robust fourfold degenerate nodal lines along the other two edge lines $U - R$ and $T - R$. Intriguingly, by taking the compactness of the BZ into account, the above-mentioned nodal lines actually form an exotic fourfold degenerate nodal net.

An example: $Pbca$ AgF_2 . Here, we take $Pbca$ AgF_2 as an example to justify the above analysis, with the corresponding crystal structure and BZ shown in Fig. 2a, b, respectively.

From the first-principles calculation, $Pbca$ AgF_2 has slightly higher energy (8 meV/Atom) than the $P21/c$ AgF_2 phase, which indicates AgF_2 in the space group of $Pbca$ may be a meta-stable phase. To check the thermal stability of $Pbca$ AgF_2 , we have performed ab initio molecular dynamic simulations at ambient pressure and $T = 600$ K. As shown in Fig. 1b in the Supplementary Material, no structural collapse was observed after 10 ps (10,000 steps), which indicates the thermal stability of AgF_2 at elevated temperature. (More details are provided in the first section of the supplementary material.)

From the fat-band structures of the $Pbca$ AgF_2 without SOC shown in Fig. 3, we can find that bands along $Z - T - Y - S - X - U$ and $U - R$ are in good agreement with the nodal surfaces and fourfold nodal lines, respectively.

Glide-mirror-symmetry-protected nodal chain and nodal armillary sphere penetrating the BZ

More interestingly, we can find two more unusual band crossings consist of F-p and Ag-d orbitals along $X - \Gamma - Z$ in the bands near the Fermi level. In fact, two-dimensional scanings of the band structures in the $k_{x,y,z} = 0$ planes show that there exist a nodal ring and a nodal armillary sphere penetrating the BZ in this system. As shown in Fig. 4a, we find three nodal rings encircling $Z - T/X - U/$

$X-S$ lines in the nattier blue/pink/green planes ($k_{x,y,z}=0$), respectively.

To obtain further insights of the above-mentioned nodal rings, we develop a two-band Hamiltonian in the bases of F-p and Ag-d orbits to depict the nodal rings locating on $k_z=0$ plane as an example. The general effective Hamiltonian can be written as

$$H(\vec{k}) = g_0(\vec{k})\tau_0 + g_x(\vec{k})\tau_x + g_y(\vec{k})\tau_y + g_z(\vec{k})\tau_z, \quad (2)$$

which satisfies

$$\tilde{M}_z H(k_x, k_y, -k_z) \tilde{M}_z^{-1} = H(k_x, k_y, k_z). \quad (3)$$

Here, the τ_x , τ_y and τ_z are Pauli matrices, τ_0 is a 2×2 unit matrix. This system has both TRS and inversion symmetry (IS), which requires the component of τ_y must be zero.¹⁶ From the ab initio calculations, we find the mirror eigenvalues of the two bands on the \tilde{M}_z invariant plane are opposite, i.e., $\tilde{M}_z = \pm \tau_z$. Thus, from Eq. 3, we find

$$\begin{aligned} g_x(k_x, k_y, -k_z) &= -g_x(k_x, k_y, k_z) \\ g_z(k_x, k_y, -k_z) &= g_z(k_x, k_y, k_z), \end{aligned} \quad (4)$$

which gives $g_x = Ak_z$ and $g_z(\vec{k}) = M - Bk_x^2 - Ck_y^2 - Dk_z^2$ up to the second order of \vec{k} . Furthermore, first-principles calculations give $M \cdot B > 0 \cap M \cdot C > 0 \cap M \cdot D > 0$, which indicates the band inversion of Ag-d and F-p orbits. Band crossings of the nodal lines will occur when $g_x = g_z = 0$. It's clear that the intersection between the nodal ellipsoid derived by $g_z(\vec{k}) = 0$ and nodal surface derived by $g_x(k) = 0$ gives the nodal ring in the $k_z=0$ plane. Similarly, two other nodal rings in the $k_{x,y}=0$ planes are also protected by the corresponding glide-mirror symmetries. It should be noted that this nodal ring still exists even when the glide-mirror symmetry is

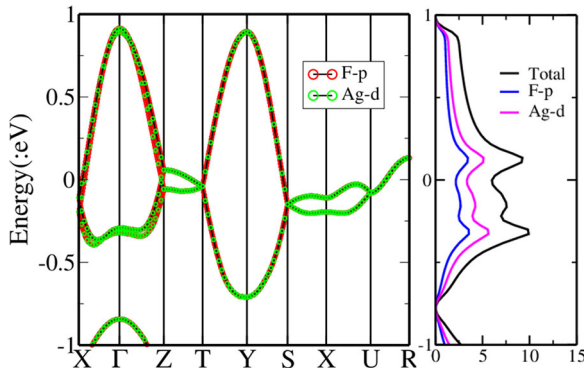


Fig. 3 Fat-band structures of *Pbca* AgF₂ without SOC, the right panel is the corresponding density of states near the Fermi level

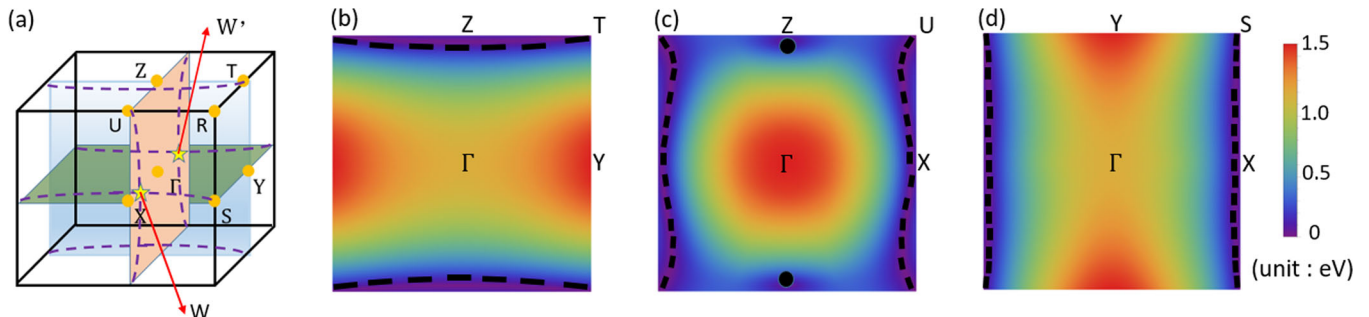


Fig. 4 The schematic figure of the nodal chain and nodal armillary sphere penetrating the Brillouin zone (BZ). **a** The nattier blue, orange, and green planes represent the $k_x=0$, $k_y=0$ and $k_z=0$ planes, respectively, while six purple-dashed arcs represent nodal lines lying in the $k_{x,y,z}=0$ planes. Take the periodicity of the BZ into consideration, then two arcs lying in $k_x=0$ plane and the other four lying in $k_{y,z}=0$ planes seem to be a nodal ring and a nodal armillary sphere penetrating the BZ respectively. The color maps in **b-d** show the direct gap between the two crossing band in the $k_{x,y,z}=0$ planes respectively from the first-principles calculations

broken, as long as the combined symmetry of TRS and IS is preserved. However, the nodal ring is no longer distributed on the glide-mirror invariant planes but in the whole three-dimensional BZ, such as the CaP₃ family.⁸⁴

Furthermore, the nodal ring in the pink plane touches the one in the green plane at W and W' , which forms the nodal armillary sphere. Owing to the compactness of the BZ, we note that the above-mentioned nodal structures are topologically distinct from those usual ones restricted within the BZ, i.e., nodal rings encircling $Z-T$, $X-S$ and $X-U$ lines are in fact nodal chains consisting of two nodal lines touching at T , S , and U , respectively. Taking the compactness into consideration, the three-dimensional BZ is topologically equivalent to a three-dimensional torus \mathbb{T}^3 .

On one hand, closed loops in \mathbb{T}^3 can be classified under its fundamental (one-dimensional) homotopy group $\pi_1(\mathbb{T}^3) = \mathbb{Z}^3$. Each of the three integers here indicates the number of times the loop winds around the BZ along one of the three directions. Similar with both nodal loops in the nanostructured carbon allotropes⁸² and CmCm K₃P₄,⁵⁰ in this system, the nodal chain lying in the $k_x=0$ plane belongs to the $2 \times \mathbb{Z}^3 = 2 \times (010)$ class while the nodal armillary sphere belongs to the $2 \times \mathbb{Z}^3 \oplus 2 \times \mathbb{Z}^3 = 2 \times (001) \oplus 2 \times (100)$ class. The number “2” is based on the fact that both the nodal chain and armillary sphere are composed of two nodal loops related to each other by the TRS or the IS.

On the other hand, the novel nodal loops above-mentioned can be also understood from the $\{BS\}$, i.e., a set of numbers of each irreducible representation at the high-symmetry \vec{k} points, though the conventional symmetry indicators^{85–87} can not be defined for TSMs with the band crossings passing through high-symmetry points. For the nodal chain in the $k_a=0$ plane, $n_{K_y}^+ - n_{\Gamma}^+ = 1$ indicates the existence of the nodal loop, while more importantly, $n_{K_y}^+ - n_{K_{\beta y}}^+ = 0$ indicates the nodal loop traverses the BZ along the k_{β} direction. In the above, $n_{K_y}^+$ represents the number of occupied bands with $+e^{-i\frac{k_{\beta}}{2}}$ glide-mirror eigenvalue at $\{K_{\alpha}, K_{\beta}, K_{\gamma}\} = \{0, 0, \pi\}$, while $K_{\beta y}$ represents the momentum infinitely close to $\{K_{\alpha}, K_{\beta}, K_{\gamma}\} = \{0, \pi, \pi\}$ along the $k_a=0 \cap k_y=\pi$ line, respectively.

At last, following the analysis in the works,^{88,89} we emphasize that the inclusion of SOC will break the SU(2) symmetry and induce a full gap in $k_x=0$ plane. Nevertheless, since SOC-induced gap is very small (<8 meV) from first-principles calculations, *Pbca* AgF₂ still serves as a good candidate with intriguing band crossings in the form of nodal chain and nodal armillary sphere penetrating the BZ.

Nodal phenomena with SOC: fourfold degenerate nodal lines and hourglass Dirac loops

When SOC is considered, the symmetry-enforced band crossings will be strongly modified due to the fact that the glide-mirror

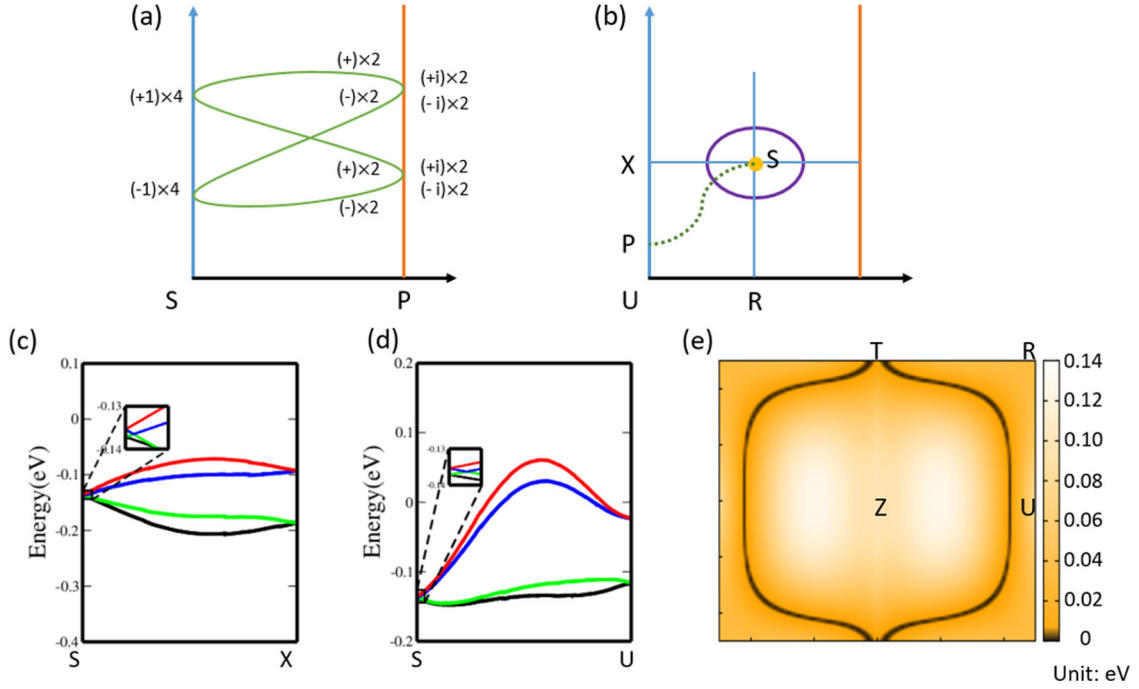


Fig. 5 The formation mechanism of the hourglass Dirac loops locating in $k_{x,y,z} = \pi$ planes. **a** The schematic figure of hourglass dispersion along an arbitrary path on $k_x = \pi$ plane connecting S to any point (signed as P) on U–X. Labels in the figure represent \tilde{M}_x eigenvalue. We can find the fourfold-degenerate crossing due to partner switching between two quartets. **b** Such crossing traces out a Dirac loop (signed as a purple ellipse). From band structure along **c** S–X and **d** S–U on $k_x = \pi$ plane, we can find that Dirac loop on this plane is very small. **e** The color map shows the direct gap between the two crossing bands on the $k_z = \pi$ plane, which indicates two clear hourglass Dirac loops traversing the BZ on this plane

symmetries, the skew axis symmetries and TRS now operate also on the spin space.

Firstly, it is easy to show that $k_\alpha = \pi \cap k_\beta = 0$ lines with $(\alpha, \beta) = \{x, y, z\}$, i.e., $X-U$, $Y-S$ and $Z-T$, are three fourfold degenerate edge lines, similar with the analysis of hourglass Dirac chain states in ReO_2 ⁹⁰ (see the supplementary material for more details).

In the following, we will focus on the high-symmetry line $X-S$ ($k_x = \pi \cap k_z = 0$), which is both \tilde{M}_x and \tilde{M}_z invariant. Owing to the commutation relation $[\tilde{G}_x, \tilde{G}_z] = 0$, we can choose each state on this line as the simultaneous eigenstate of both glide-mirror operators with the corresponding eigenvalue $\{g_x, g_z\}$. Since $\tilde{M}_x^2 = -T_{010}$ and $\tilde{M}_z^2 = -T_{100} = -e^{-ik_x} = 1$, we have $\{g_x, g_z\} = \{\pm ie^{-\frac{ik_x}{2}}, \pm 1\}$. Assume $|\mu\rangle$ is the eigenstate with $\{g_x, g_z\} = \{ie^{-\frac{ik_x}{2}}, 1\}$ and make use of Eq. (8) in the supplementary material, we find

$$\begin{aligned} \tilde{M}_x PT|\mu\rangle &= P\tilde{M}_x T_{110} T|\mu\rangle = e^{-i(k_x+k_y)} PT\tilde{M}_x|\mu\rangle \\ &= -e^{-ik_y} PTie^{-\frac{ik_x}{2}}|\mu\rangle = ie^{-\frac{ik_x}{2}} PT|\mu\rangle, \\ \tilde{M}_z PT|\mu\rangle &= P\tilde{M}_z T_{101} T|\mu\rangle = -PT|\mu\rangle. \end{aligned} \quad (5)$$

It means locally degenerate states related to each other by P^*T symmetry have the same \tilde{M}_x eigenvalue and opposite \tilde{M}_z eigenvalues, i.e.,

$$\begin{aligned} (\tilde{M}_x, \tilde{M}_z)|\mu\rangle &= (g_x, g_z)|\mu\rangle \\ (\tilde{M}_x, \tilde{M}_z)PT|\mu\rangle &= (g_x, -g_z)|\mu\rangle. \end{aligned} \quad (6)$$

Additionally, at the time-reversal-invariant momentum $X(\pi, 0, 0)$, for the state $|\mu\rangle$ with $(g_x, g_z) = (\pm i, \pm 1)$, its Kramers partner $T|\mu\rangle$ must have eigenvalue $(-g_x, g_z)$. Similarly, at the $S(\pi, \pi, 0)$ point, we have $(g_x, g_z) = (\pm 1, \pm 1)$, hence the corresponding Kramers partner $T|\mu\rangle$ have the same eigenvalue as $|\mu\rangle$. Focus on the eigenvalue g_x , the four states (can be chosen as $|\mu\rangle, T|\mu\rangle, P|\mu\rangle, PT|\mu\rangle$) formed in the degenerate quartet at X consists of two states with $g_x = i$ while the other two states with $g_x = -i$. However, at S, the four states in

the degenerate quartet all have the same g_x (+1 or -1). Consequently, there must exist a switch of partners between two quartets along $X-S$, which forms an hourglass-type dispersion, as shown in Fig. 5a. Furthermore, we notice that the whole $k_x = \pi$ plane is \tilde{M}_x invariant, which means g_x is well defined in this plane. Thus, similar with the above-mentioned discussion, any path lying on the $k_x = \pi$ plane connecting X and S must feature an hourglass dispersion with fourfold degenerate crossings in between. The crossing points must trace out a closed Dirac loop on this plane, as shown in Fig. 5b.

In fact, it should be noted that not only X, but actually any point P on line $X-U$ are fourfold degenerate states, namely, two with $g_x = +i$ and the other two with $g_x = -i$. As a result, the hourglass spectrum is guaranteed to appear on any path connecting S to an arbitrary point on $U-X$.

According to the cyclic permutation relation, there exist two other hourglass spectra on the $k_y = \pi$ and $k_z = \pi$ planes, respectively. In a word, there exist three hourglass Dirac loops surrounding $S/T/U$ point on the $k_{x,y,z} = \pi$ plane.

The first-principles calculations show that hourglass Dirac loops in the $k_x = \pi$ and $k_y = \pi$ planes are a little ambiguous, i.e., the radius of both the two loops surrounding S and T points are very small. We have also chosen the hourglass Dirac loop in the $k_x = \pi$ as an example, which can be clearly seen from the insets of Fig. 5c, d. Furthermore, as shown in Fig. 5e, there exist two hourglass Dirac loops traversing the BZ in the $k_z = \pi$ plane. It can be classified as type-II hourglass Dirac loop with $2 \times Z^3 = 2 \times (100)$, which is different from the general $Z^3 = (000)$ class. Similar with the nodal chain and nodal armillary sphere penetrating the BZ, the type-II hourglass Dirac loop in the $k_z = \pi$ plane can be also understood from the {BS}. We introduce a new index as $Z_2 = \frac{n_U^+ - n_B^+}{2} \bmod 2$, and $Z_2 = 0$ gives the type-II hourglass Dirac loop for this half-filled system with the number of the electrons $132 = 8 \times n + 4$, while \mathbb{U} represents the momentum infinitely

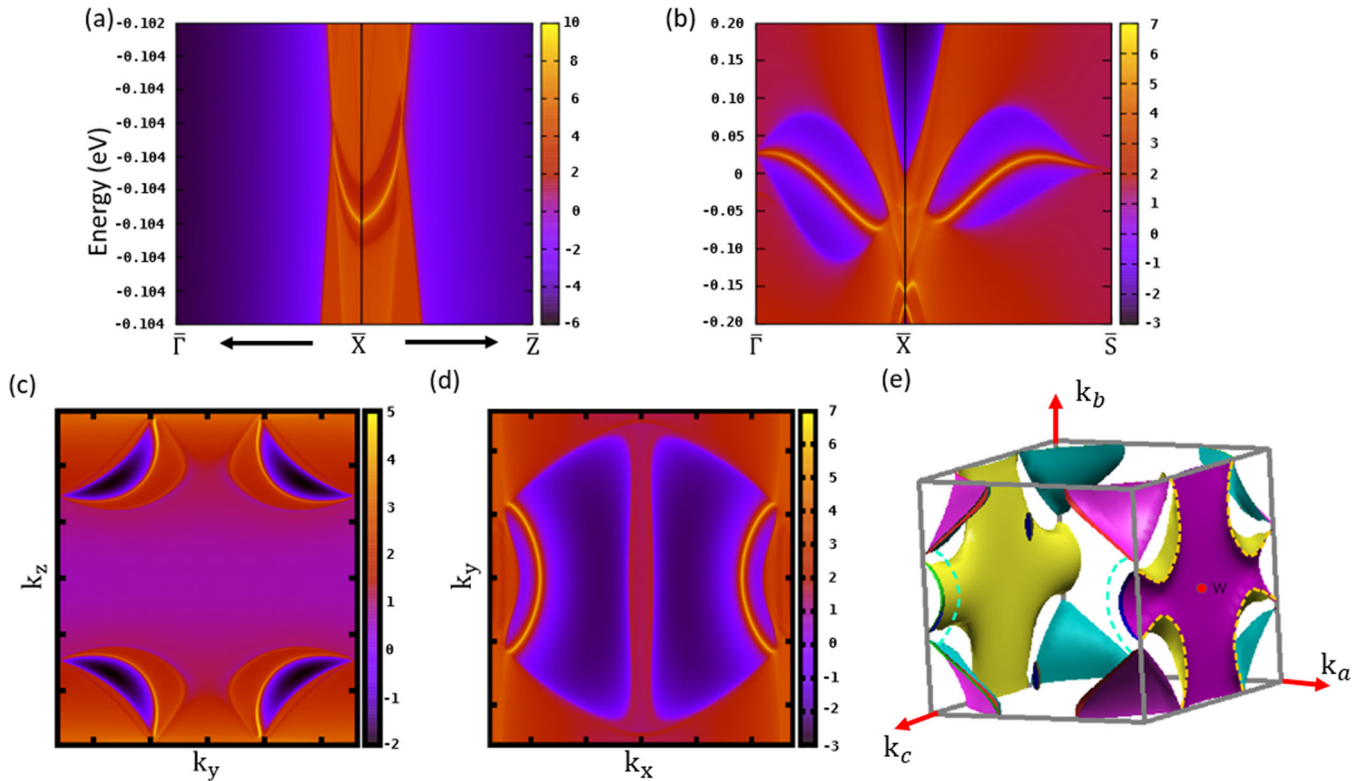


Fig. 6 The surface states without SOC of *Pbca* AgF_2 along the **a** [010] and **b** [001] directions, respectively. The Fermi arcs projected along **c** [100] and **d** [001] directions, respectively. **e** The corresponding Fermi surface. The bright dashed orange and blue curves in the Fermi surface respect the corresponding Fermi circles along [100] and [001] directions, respectively

close to U along the $U-R$ line. More interestingly, as shown in Fig. 7a, the type-II hourglass Dirac loop touches another hourglass Dirac loop in the $k_y = \pi$ plane, leading to the formation of a novel hourglass Dirac chain traversing the BZ.

Surface states

Exotic topological surface states serve as significant fingerprints to identify various topological phases. Based on the tight-binding model constructed with the maximally localised Wannier functions and surface Green function methods,^{91–93} we have calculated the corresponding surface states and Fermi arcs of this system without SOC to identify these fancy nodal features. There is always one nodal chain in the two-dimensional projected BZ, no matter which direction is chosen to be orthogonal to the surface. Projected nodal points from the three-dimensional BZ may exhibit Fermi-arc surface states.

As shown in Fig. 6a, b, projected surface states along [010] and [001] directions reveal that the drumhead-like surface bands nestle inside the circles formed by bulk bands. As the blue and red closed loops show in Fig. 6a, there exist bright surface states connecting two projected nodal points located in the armillary sphere near the \bar{X} point. While surface states along [001] direction consisting of two arcs along the $\bar{X}-\bar{\Gamma}$ and $\bar{X}-\bar{S}$ paths are much larger, as shown in Fig. 6b. On the other hand, Fermi arcs projected to [100] and [001] directions are found in Fig. 6c, d, respectively. Taking the compactness of the BZ into consideration, the Fermi arcs projected to [100] direction emitting from fourfold degenerate nodes at the axis of BZ near the Fermi level form a closed Fermi circle while the ones along [001] direction coincidentally stay separately from the bulk Fermi surface at [001] surface, which are illustrated as bright dashed orange and blue curves in the Fermi surface in Fig. 6e, respectively.

Table 2. The effect of tetragonal and cubic uniaxial strain of the lattice parameters

Strains	a, b, c	$a = \beta = \gamma$
Tetragonal	$a = 5.529$ (Å), $b = c = 5.43$ (Å)	90°
Cubic	$a = b = c = 5.463$ (Å)	90°

From the above-mentioned, the hourglass Dirac loop in the $k_z = \pi$ plane splits into two loops traversing the BZ when SOC is considered. The corresponding surface states with SOC along [001] direction are also presented (the detail is shown in Fig. 3 of the supplementary text).

Evolution of the nodal phenomena under uniaxial strains

As known to all, symmetries play key roles on the topological phase and topological phase transitions. It is interesting that uniaxial strain along x , y , and z directions will preserve all symmetries of this system. As a result, both symmetry-enforced nodal surface and fourfold degenerate nodal lines encircling the whole BZ without SOC are preserved under uniaxial strains. However, what is the fate of the nodal chain, nodal armillary sphere and hourglass Dirac chain penetrating the BZ under the uniaxial strain, respectively? Here, we have chosen two special uniaxial strains with fixed volume to explore the potential phase transition. We call the uniaxial strains as the tetragonal and cubic strains respectively, which modify the lattice parameters as Table 2 shows.

In the absence of SOC: nodal chain and nodal armillary sphere penetrating the BZ

First-principles calculations indicate both strains will “push” the nodal chain in the $k_x = 0$ plane to the edge, while “push” the nodal

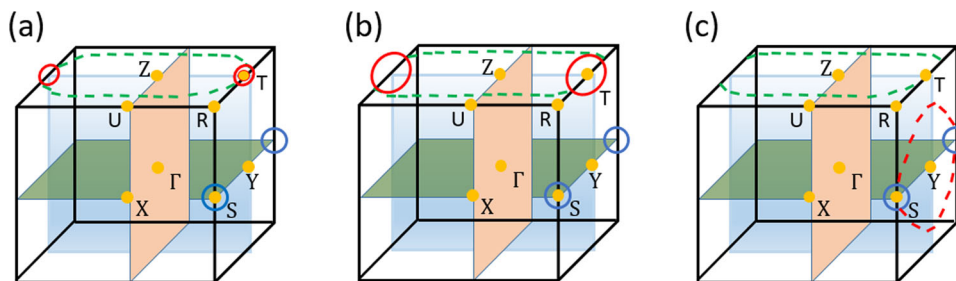


Fig. 7 The schematic figures represent the evolution of the hourglass Dirac chain penetrating the Brillouin zone (BZ) under uniaxial strain. The solid closed loops and dashed lines represent the hourglass Dirac loops confined and transverse the BZ in $k_{x,y,z} = \pi$ planes, respectively. **a** Without strain, the hourglass Dirac chain is composed of the red closed loop and the green dashed lines transverse the BZ. **b** The red closed loop enlarges under the tetragonal uniaxial strain. **c** Under the cubic uniaxial strain, the red closed loop continues to enlarge across the R point (i.e., traverse the BZ), then touches with the blue closed loops. As a result, a new hourglass Dirac chain appears while the old chain disappears

armillary sphere to the center (the Γ point). Fortunately, the nodal chain and nodal armillary sphere penetrating the BZ are still preserved, which indicates they are very stable against the uniaxial strains.

In the presence of SOC: hourglass Dirac chains traversing the BZ. It is obvious that both SOC and the band inversion play an important role on the formation of the novel hourglass Dirac loops/chain in this system. As shown in Fig. 7b, we find all the hourglass Dirac loops are preserved, and the only difference is that the small red hourglass Dirac loop on $k_y = \pi$ enlarges under the tetragonal uniaxial strain. Furthermore, under the cubic uniaxial strain, the red closed loop continues to enlarge and goes across the R point (i.e., traverses the BZ), then touches the blue closed loops. As a result, a new hourglass Dirac chain traversing the BZ appears while the old one disappears.

At last, we have also performed calculations to discuss the evolution of the hourglass Dirac chain with gradually increased SOC magnitude (25, 50, 75, 100%), which indicates the magnitude of SOC only changes the size of the hourglass Dirac loop and chain, but the nodal feature traversing the BZ is preserved. More details are discussed in the supplementary material.

In conclusion, based on the symmetry analysis, we propose that systems with TRS in the space group of $Pbca$ (No. 61) possess rich band-crossing features. Without SOC, there exist three symmetry-enforced nodal surfaces and fourfold degenerate nodal lines surrounding all the surfaces and the edge ridges of the BZ, respectively. When SOC is taken into consideration, there must exist a hourglass Dirac loop on each surface of the BZ. It should be noted that all of the above-mentioned nodal phenomena appear in triplet as a result of the cyclic permutation of the symmetries in these systems. We have chosen AgF_2 as an example to justify the above-mentioned symmetry-enforced nodal phenomena making use of both first-principles calculations and tight-binding model analysis. Unprecedentedly, without SOC, we find additional nodal chain and nodal armillary sphere penetrating the BZ. Furthermore, when SOC is taken into consideration, we find the hourglass Dirac loops in the $k_z = \pi$ plane traverse the BZ and touch with the one in the $k_y = \pi$ plane, which forms a novel hourglass Dirac chain traversing the BZ. The novel surface states have also been presented to further support the analysis of bulk-band topology. At last, we show the evolution of all the novel nodal phenomena traversing the BZ under two specific uniaxial strains, which respect the $Pbca$ symmetry. It should be emphasized that the rich nodal features make this system quite distinctive, which provides a significant platform to explore intriguing physics in topological materials.

METHODS

We performed first-principles calculations based on the density functional theory (DFT) using the full-potential linearized augmented plane-wave (FP-LAPW) method^{94,95} implemented in the WIEN2k⁹⁶ package. We use $13 \times 9 \times 11$ k-mesh for the BZ sampling and -7 for the plane-wave cut-off parameter $R_{MT}K_{max}$ for the calculation of the band structure, where the R_{MT} is the minimum muffin-tin radius and K_{max} is the plane-wave vector cutoff parameter. SOC is taken into consideration by a second-variation method⁹⁷. The projected surface states are calculated using surface Green's function in the semi-infinite system implemented in the wannier90 code^{94,92}, the corresponding tight-binding models are constructed with the maximally localized Wannier functions (MLWFs) method^{98–100}.

DATA AVAILABILITY

The datasets used in this article are available from the corresponding author upon request.

ACKNOWLEDGEMENTS

We thank for the fruitful discussions with Chen Fang, Shengyuan Yang, Jiawei Ruan, and Di Wang. In addition, Dexi Shao wants to thank Ting Sun. At last, we thank for the financial support from MOST of China (Grant Nos: 2016YFA0300404 and 2015CB921202), the National Natural Science Foundation of China (Grant Nos: 11574133, 11834006), the NSF Jiangsu province in China (No. BK201500012), the Fundamental Research Funds for the Central Universities and the program B for Outstanding Ph.D candidate of Nanjing University. Calculations were performed on the computing facilities in the High Performance Computing Center (HPCC) of Nanjing University and "Tianhe-2" at NSCC-Guangzhou.

AUTHOR CONTRIBUTIONS

J.S. and D.S. designed this project. D.S. performed the calculations. J.S. and D.S. made the analysis and wrote the manuscript. All authors discussed the results and commented on the manuscript.

ADDITIONAL INFORMATION

Supplementary information accompanies the paper on the *npj Computational Materials* website (<https://doi.org/10.1038/s41524-019-0190-3>).

Competing interests: The authors declare no competing interests.

Publisher's note: Springer Nature remains neutral with regard to jurisdictional claims in published maps and institutional affiliations.

REFERENCES

- Hasan, M. Z. & Kane, C. L. Colloquium: Topological insulators. *Rev. Mod. Phys.* **82**, 30453067 (2010).
- Qi, X.-L. & Zhang, S.-C. Topological insulators and superconductors. *Rev. Mod. Phys.* **83**, 1057–1110 (2011).

3. Armitage, N. P., Mele, E. J. & Vishwanath, A. Weyl and Dirac semimetals in three-dimensional solids. *Rev. Mod. Phys.* **90**, 015001 (2018).
4. Kane, C. L. & Mele, E. J. Quantum Spin Hall effect in graphene. *Phys. Rev. Lett.* **95**, 226801 (2005).
5. Wan, X., Turner, A. M., Vishwanath, A. & Savrasov, S. Y. Topological semimetal and fermi-arc surface states in the electronic structure of pyrochlore iridates. *Phys. Rev. B* **83**, 205101 (2011).
6. Xu, G., Weng, H., Wang, Z., Dai, X. & Fang, Z. Chern semimetal and the quantized anomalous Hall effect in HgCr_2Se_4 . *Phys. Rev. Lett.* **107**, 186806 (2011).
7. Yang, K.-Y., Lu, Y.-M. & Ran, Y. Quantum Hall effects in a weyl semimetal: Possible application in pyrochlore iridates. *Phys. Rev. B* **84**, 075129 (2011).
8. Burkov, A. A. & Balents, L. Weyl semimetal in a topological insulator multilayer. *Phys. Rev. Lett.* **107**, 127205 (2011).
9. Burkov, A. A., Hook, M. D. & Balents, L. Topological nodal semimetals. *Phys. Rev. B* **84**, 235126 (2011).
10. Halász, G. B. & Balents, L. Time-reversal invariant realization of the weyl semimetal phase. *Phys. Rev. B* **85**, 035103 (2012).
11. Zyuzin, A. A., Wu, S. & Burkov, A. A. Weyl semimetal with broken time reversal and inversion symmetries. *Phys. Rev. B* **85**, 165110 (2012).
12. Lu, L., Fu, L., Joannopoulos, J. & Soljacic, M. Weyl points and line nodes in gapless gyroid photonic crystals. *Nat. Photon.* **7**, 294–299 (2012).
13. Das, T. Weyl semimetal and superconductor designed in an orbital-selective superlattice. *Phys. Rev. B* **88**, 035444 (2013).
14. Liu, J. & Vanderbilt, D. Weyl semimetals from noncentrosymmetric topological insulators. *Phys. Rev. B* **90**, 155316 (2014).
15. Zhang, H., Wang, J., Xu, G., Xu, Y. & Zhang, S.-C. Topological states in ferromagnetic CdO/EuO superlattices and quantum wells. *Phys. Rev. Lett.* **112**, 096804 (2014).
16. Weng, H., Fang, C., Fang, Z., Bernevig, B. A. & Dai, X. Weyl semimetal phase in noncentrosymmetric transition-metal monophosphides. *Phys. Rev. X* **5**, 011029 (2015).
17. Xu, S.-Y. et al. Discovery of a weyl fermion semimetal and topological fermi arcs. *Science* **349**, 613–617 (2015).
18. Lv, B. Q. et al. Experimental discovery of weyl semimetal TaAs. *Phys. Rev. X* **5**, 031013 (2015).
19. Yang, L. X. et al. Weyl semimetal phase in the non-centrosymmetric compound TaAs. *Nat. Phys.* **11**, 879–879 (2015).
20. Lv, B. Q. et al. Observation of weyl nodes in TaAs. *Nat. Phys.* **11**, 724 (2015).
21. Xu, S.-Y. et al. Experimental discovery of a topological weyl semimetal state in TaP. *Sci. Adv.* **1**, e1501092 (2015).
22. Alidoust, N. et al. Discovery of a weyl fermion state with fermi arcs in niobium arsenide. *Nat. Phys.* **11**, 748–754 (2015).
23. Huang, S.-M. et al. A weyl fermion semimetal with surface fermi arcs in the transition metal monpnictide TaAs class. *Nat. Commun.* **6**, 7373 (2015).
24. Xu, N. et al. Observation of weyl nodes and fermi arcs in tantalum phosphide. *Nat. Commun.* **7**, 11006 (2016).
25. Lu, L. et al. Experimental observation of weyl points. *Science* **349**, 622–624 (2015).
26. Ruan, J. et al. Symmetry-protected ideal weyl semimetal in HgTe-class materials. *Nat. Commun.* **7**, 11136 (2016).
27. Ruan, J. et al. Ideal weyl semimetals in the chalcopyrites CuTiSe_2 , AgTiTe_2 , AuTiTe_2 , and ZnPbAs_2 . *Phys. Rev. Lett.* **116**, 226801 (2016).
28. Wang, Z. et al. Dirac semimetal and topological phase transitions in A_3Bi ($\text{A} = \text{Na}, \text{K}, \text{Rb}$). *Phys. Rev. B* **85**, 195320 (2012).
29. Young, S. M. et al. Dirac semimetal in three dimensions. *Phys. Rev. Lett.* **108**, 140405 (2012).
30. Wang, Z., Weng, H., Wu, Q., Dai, X. & Fang, Z. Three-dimensional Dirac semimetal and quantum transport in Cd_3As_2 . *Phys. Rev. B* **88**, 125427 (2013).
31. Liu, Z. K. et al. A stable three-dimensional topological Dirac semimetal Cd_3As_2 . *Nat. Mater.* **13**, 677 (2014).
32. Chen, Y. L. et al. Discovery of a three-dimensional topological Dirac semimetal, Na_3Bi . *Science* **343**, 864–867 (2014).
33. Neupane, M. et al. Observation of a three-dimensional topological Dirac semimetal phase in high-mobility Cd_3As_2 . *Nat. Commun.* **5**, 3786 (2014).
34. Yang, B. J. & Nagaosa, N. Classification of stable three-dimensional Dirac semimetals with nontrivial topology. *Nat. Commun.* **5**, 4898–4898 (2014).
35. Xu, S. Y. et al. Observation of Fermi arc surface states in a topological metal. *Science* **347**, 294–298 (2015).
36. Young, S. M. & Kane, C. L. Dirac semimetals in two dimensions. *Phys. Rev. Lett.* **115**, 126803 (2015).
37. Xu, C.-Z. et al. Elemental topological Dirac semimetal: $\alpha\text{-Sn}$ on $\text{InSb}(111)$. *Phys. Rev. Lett.* **118**, 146402 (2017).
38. Huang, H. & Liu, F. Tensile strained gray tin: Dirac semimetal for observing negative magnetoresistance with Shubnikov-de Haas oscillations. *Phys. Rev. B* **95**, 201101 (2017).
39. Tang, P., Zhou, Q., Xu, G. & Zhang, S.-C. Dirac fermions in an antiferromagnetic semimetal. *Nat. Phys.* **12**, 1100 (2016).
40. Wang, J. Antiferromagnetic Dirac semimetals in two dimensions. *Phys. Rev. B* **95**, 115138 (2017).
41. Zhang, D., Wang, H., Ruan, J., Yao, G. & Zhang, H. Engineering topological phases in the Luttinger semimetal $\alpha\text{-Sn}$. *Phys. Rev. B* **97**, 195139 (2018).
42. Hua, G. et al. Dirac semimetal in type IV magnetic space group. *arXiv:1801.02806* (2018).
43. Zhang, J. et al. Topological band crossings in hexagonal materials. *Phys. Rev. Mater.* **2**, 074201 (2018).
44. Yu, R., Weng, H., Fang, Z., Dai, X. & Hu, X. Topological node-line semimetal and Dirac semimetal state in antiperovskite Cu_3PdN . *Phys. Rev. Lett.* **115**, 036807 (2015).
45. Kim, Y., Wieder, B. J., Kane, C. L. & Rappe, A. M. Dirac line nodes in inversion-symmetric crystals. *Phys. Rev. Lett.* **115**, 036806 (2015).
46. Bian, G. et al. Drumhead surface states and topological nodal-line fermions in TiTaSe_2 . *Phys. Rev. B* **93**, 121113 (2016).
47. Fang, C., Weng, H., Dai, X. & Fang, Z. Topological nodal line semimetals. *Chin. Phys. B* **25**, 9–18 (2016).
48. Yu, R., Fang, Z., Dai, X. & Weng, H. Topological nodal line semimetals predicted from first-principles calculations. *Front. Phys.* **12**, 127202 (2017).
49. Yan, Z. et al. Nodal-link semimetals. *Phys. Rev. B* **96**, 041103 (2017).
50. Li, S. et al. Type-II nodal loops: Theory and material realization. *Phys. Rev. B* **96**, 081106 (2017).
51. Sun, Y., Zhang, Y., Liu, C.-X., Felser, C. & Yan, B. Dirac nodal lines and induced spin Hall effect in metallic rutile oxides. *Phys. Rev. B* **95**, 235104 (2017).
52. Chen, W., Lu, H.-Z. & Hou, J.-M. Topological semimetals with a double-helix nodal link. *Phys. Rev. B* **96**, 041102 (2017).
53. Chang, G. et al. Topological Hopf and chain link semimetal states and their application to Co_2MnGa . *Phys. Rev. Lett.* **119**, 156401 (2017).
54. Liang, Q.-F., Zhou, J., Yu, R., Wang, Z. & Weng, H. Node-surface and node-line fermions from nonsymmorphic lattice symmetries. *Phys. Rev. B* **93**, 085427 (2016).
55. Zhong, C. et al. Towards three-dimensional Weyl-surface semimetals in graphene networks. *Nanoscale* **8**, 7232 (2016).
56. Bzdušek, Tcv & Sigrist, M. Robust doubly charged nodal lines and nodal surfaces in centrosymmetric systems. *Phys. Rev. B* **96**, 155105 (2017).
57. Guan, S. et al. Two-dimensional spin-orbit Dirac point in monolayer HfGeTe . *Phys. Rev. Mater.* **1**, 054003 (2017).
58. Wu, W. et al. Nodal surface semimetals: Theory and material realization. *Phys. Rev. B* **97**, 115125 (2018).
59. Schnyder, A. P., Ryu, S., Furusaki, A. & Ludwig, A. W. W. Classification of topological insulators and superconductors in three spatial dimensions. *Phys. Rev. B* **78**, 195125 (2008).
60. Kitaev, A. Periodic table for topological insulators and superconductors. *AIP Conf. Proc.* **1134**, 22–30 (2009).
61. Fu, L. Topological crystalline insulators. *Phys. Rev. Lett.* **106**, 106802 (2011).
62. Slager, R.-J., Mesaros, A., Juricic, V. & Zaanen, J. The space group classification of topological band insulators. *Nat. Phys.* **9**, 98 (2013).
63. Jadaun, P., Xiao, D., Niu, Q. & Banerjee, S. K. Topological classification of crystalline insulators with space group symmetry. *Phys. Rev. B* **88**, 085110 (2013).
64. Shiozaki, K. & Sato, M. Topology of crystalline insulators and superconductors. *Phys. Rev. B* **90**, 165114 (2014).
65. Wang, Z., Alexandradinata, A., Cava, R. J. & Bernevig, B. A. Hourglass Fermions. *Nature* **532**, 189–194 (2016).
66. Fang, C., Gilbert, M. J., Dai, X. & Bernevig, B. A. Multi-weyl topological semimetals stabilized by point group symmetry. *Phys. Rev. Lett.* **108**, 266802 (2012).
67. Bradlyn, B. et al. Beyond Dirac and Weyl Fermions: Unconventional quasiparticles in conventional crystals. *Science* **353**, aaf5037 (2016).
68. Wieder, B. J., Kim, Y., Rappe, A. M. & Kane, C. L. Double Dirac semimetals in three dimensions. *Phys. Rev. Lett.* **116**, 186402 (2016).
69. Liu, Q. & Zunger, A. Predicted realization of cubic Dirac Fermion in quasi-one-dimensional transition-metal monochalcogenides. *Phys. Rev. X* **7**, 021019 (2017).
70. Haldane, F. D. M. Attachment of surface “Fermi arcs” to the bulk Fermi surface: “Fermi-level plumbing” in topological metals. *arXiv:1401.0529v1* (2014).
71. Nielsen, H. & Ninomiya, M. A no-go theorem for regularizing chiral Fermions. *Phys. Lett. B* **105**, 219–223 (1981).
72. Liu, C.-X., Ye, P. & Qi, X.-L. Chiral gauge field and axial anomaly in a Weyl semimetal. *Phys. Rev. B* **87**, 235306 (2013).
73. Son, D. T. & Spivak, B. Z. Chiral anomaly and classical negative magnetoresistance of Weyl metals. *Phys. Rev. B* **88**, 104412 (2013).
74. Hosur, P. & Qi, X. Recent developments in transport phenomena in Weyl semimetals. *C. R. Phys.* **14**, 857–870 (2013).
75. Xiong, J. et al. Evidence for the chiral anomaly in the Dirac semimetal Na_3Bi . *Science* **350**, 413–416 (2015).

76. Huang, X. et al. Observation of the chiral-anomaly-induced negative magnetoresistance in 3d Weyl semimetal TaAs. *Phys. Rev. X* **5**, 031023 (2015).
77. Zhang, C. L. et al. Signatures of the adler-bell-jackiw chiral anomaly in a Weyl Fermion semimetal. *Nat. Commun.* **7**, 10735 (2016).
78. Li, Q. et al. Chiral magnetic effect in ZrTe₅. *Nat. Phys.* **12**, 550–554 (2016).
79. Zyuzin, A. & Burkov, A. Topological response in Weyl semimetals and the chiral anomaly. *Phys. Rev. B* **86**, 115133 (2012).
80. Chang, M.-C. & Yang, M.-F. Chiral magnetic effect in a two-band lattice model of Weyl semimetal. *Phys. Rev. B* **91**, 115203 (2015).
81. Vazifeh, M. & Franz, M. Electromagnetic response of Weyl semimetals. *Phys. Rev. Lett.* **111**, 027201 (2013).
82. Chen, Y. et al. Nanostructured carbon allotropes with Weyl-like loops and points. *Nano. Lett.* **15**, 6974 (2015).
83. Li, S. et al. Nonsymmorphic-symmetry-protected hourglass Dirac loop, nodal line, and Dirac point in bulk and monolayer X₃SiTe₆ (X = Ta, Nb). *Phys. Rev. B* **97**, 045131 (2018).
84. Xu, Q., Yu, R., Fang, Z., Dai, X. & Weng, H. Topological nodal line semimetals in the CaP₃ family of materials. *Phys. Rev. B* **95**, 045136 (2017).
85. Po, H. C., Vishwanath, A. & Watanabe, H. Symmetry-based indicators of band topology in the 230 space groups. *Nat. Commun.* **8**, 50 (2017).
86. Song, Z., Zhang, T. & Fang, C. Diagnosis for nonmagnetic topological semimetals in the absence of spin-orbital coupling. *Phys. Rev. X* **8**, 031069 (2018).
87. Khalaf, E., Po, H. C., Vishwanath, A. & Watanabe, H. Symmetry indicators and anomalous surface states of topological crystalline insulators. *Phys. Rev. X* **8**, 031070 (2018).
88. Fang, C., Chen, Y., Kee, H.-Y. & Fu, L. Topological nodal line semimetals with and without spin-orbital coupling. *Phys. Rev. B* **92**, 081201 (2015).
89. Shao, D. et al. Nonsymmorphic symmetry protected node-line semimetal in the trigonal YH₃. *Sci. Rep.* **8**, 1467 (2018).
90. Wang, S.-S., Liu, Y., Yu, Z.-M., Sheng, X.-L. & Yang, S. A. Hourglass Dirac chain metal in rhenium dioxide. *Nat. Commun.* **8**, 1844 (2017).
91. Sancho, M. P. L., Sancho, J. M. L. & Rubio, J. Quick iterative scheme for the calculation of transfer matrices: application to Mo (100). *J. Phys. F:Met. Phys.* **14**, 1205 (1984).
92. Sancho, M. P. L., Sancho, J. M. L., Sancho, J. M. L. & Rubio, J. Highly convergent schemes for the calculation of bulk and surface green functions. *J. Phys. F:Met. Phys.* **15**, 851 (1985).
93. Wu, Q., Zhang, S., Song, H.-F., Troyer, M. & Soluyanov, A. A. Wanniertools: An open-source software package for novel topological materials. *Comput. Phys. Commun.* **224**, 405 (2018).
94. Sjöstedt, E., Nordström, L. & Singh, D. J. An alternative way of linearizing the augmented plane-wave method. *Solid State Commun.* **114**, 15–20 (2000).
95. Madsen, G. K. H., Blaha, P., Schwarz, K., Sjöstedt, E. & Nordström, L. Efficient linearization of the augmented plane-wave method. *Phys. Rev. B* **64**, 195134 (2001).
96. Blaha, P., Schwarz, K., Madsen, G., Kvasnicka, D. & Luitz, J. *WIEN2k: An Augmented Plane Wave plus Local Orbitals Program for Calculating Crystal Properties*. (Karlheinz Schwarz, Technische Universitaet Wien, Vienna, 2001).
97. Kuneš, J., Novák, P., Schmid, R., Blaha, P. & Schwarz, K. Electronic structure of fcc th: Spin-orbit calculation with $6p_{1/2}$ local orbital extension. *Phys. Rev. B* **64**, 153102 (2001).
98. Blaha, N. & Vanderbilt, D. Maximally localized generalized wannier functions for composite energy bands. *Phys. Rev. B* **56**, 12847–12865 (1997).
99. Marzari, N., Mostofi, A. A., Yates, J. R., Souza, I. & Vanderbilt, D. Maximally localized wannier functions: Theory and applications. *Rev. Mod. Phys.* **84**, 1419–1475 (2012).
100. Mostofi, A. A. et al. wannier90: A tool for obtaining maximally-localised wannier functions. *Comput. Phys. Commun.* **178**, 685–699 (2008).



Open Access This article is licensed under a Creative Commons Attribution 4.0 International License, which permits use, sharing, adaptation, distribution and reproduction in any medium or format, as long as you give appropriate credit to the original author(s) and the source, provide a link to the Creative Commons license, and indicate if changes were made. The images or other third party material in this article are included in the article's Creative Commons license, unless indicated otherwise in a credit line to the material. If material is not included in the article's Creative Commons license and your intended use is not permitted by statutory regulation or exceeds the permitted use, you will need to obtain permission directly from the copyright holder. To view a copy of this license, visit <http://creativecommons.org/licenses/by/4.0/>.

© The Author(s) 2019